



Vortex-induced Energy Harvesting of an Elliptic Blade in High-Reynolds Lid-driven Cavity Flow

Ali Akbar Hosseinjani ^{1,*}, Ghasem Akbari ¹

¹ Department of Mechanical Engineering, Qazvin Branch, Islamic Azad University, Qazvin, Iran.

Received: 02 May 2022- Accepted: 11 October 2022

*Corresponding author: aahosseinjani@qiau.ac.ir

Abstract

Lid-driven cavity flow is characterized by large-scale energetic eddies which are potential for energy harvesting purposes. The present article deals with numerical study of vortex-induced autorotation of an elliptic blade hinged at the center of a lid-driven cavity. Immersed boundary method is utilized to solve the governing equations for this moving boundary problem. Four different blade dimensions are considered at a fairly high-Reynolds number to evaluate the impact of various vortex types and flow unsteadiness on the blade dynamics. Small-amplitude fluttering, clockwise autorotation and counter-clockwise autorotation are three dominant modes observed at various configurations and different temporal stages. The average-length blade is equally characterized by vortices at both directions, and consequently experiences a fluttering mode. In contrast, short (long) blade is mainly affected by one dominant vortex type, leading to steady autorotation in counter-clockwise (clockwise) direction. At stable autorotation of blade in both directions, regular cyclic temporal oscillations are observed in the rotational speed, which are due to cyclic evolution of the near-blade vortices and their alternating moment applied to the blade.

Keywords: Lid-driven cavity; Immersed boundary method; Fluid-structure interaction; Dynamic modes; Vortex-induced autorotation.

1. Introduction

Lid-driven cavity flow is one of popular case studies in fluid dynamics community because it is characterized by simple geometry and basic fluid mechanics concepts. Boundary layer, dynamic flow patterns and shear-induced vortices are the main regimes that significantly characterize the cavity flow. Several engineering problems can be simplified by cavity flow model. Lubrication technology, cooling of electronic devices, oil extraction and solar collectors are a few examples in this regard. The main concern of the present study is energy harvesting from a lid-driven cavity by auto-rotation of an object hinged across its cellular vortices.

auto-rotation can be defined as persistent rotation of an object around a fixed axis because of the fluid stream [1]. Numerous studies have been devoted to autorotation of circular and non-circular cylinders with an axis of rotation located normal to main stream. Juarez et al. [2] considered Navier-Stokes equations coupled with the equation of angular momentum to investigate flow past a freely rotating cylinder in a channel. Xia et al. [3] utilized lattice Boltzmann method (LBM) to examine the impact of different Reynolds numbers, eccentricities and blockage ratios on free rotation of a circular cylinder asymmetrically confined in a two-dimensional channel. Anomalous clockwise rotation was the dominant behavior observed for the low blockage ratios. Such characteristic was also reported in another study for a freely rotating cylinder located eccentrically in the passage of Poiseuille flow of power-law fluid in a 2D channel [4]. The cylinder rotational speed decreased with an increase in Reynolds number (except for the low Reynolds conditions) and increased with power-law-index of the non-Newtonian fluid.

Regarding autorotation of non-circular cylinders, investigation of multi-side bodies revealed the highest rotational rate for the triangular prism, which was slightly higher than that of two- and four-side prisms [5]. Utilization of bodies with more than four sides steadily decreased the rate of rotation. Numerical and experimental study of autorotation of a freely rotatable square cylinder in a uniform flow revealed four distinct regimes for different Reynolds

numbers[6]. They involved stable position with parallel surfaces with respect to the flow, periodic oscillations, alternating rotation and steady uni-direction autorotation. Ryu[7] analysed the same configuration in order to comprehend how vortex shedding and stagnation pressure are effective in generation of moment on each side of square cylinder and sustenance of autorotation. They found adverse effects on the windward side of the cylinder, whereas the leeward side favourably assisted the net moment. Park et al. [8] utilized direct-forcing/fictitious domain method to handle fluid-structure interaction for a free-to-rotate rectangular cylinder in a uniform flow. Several ranges of Reynolds number and width to height ratio were applied to realize that periodic oscillation and autorotation are two distinct motion modes for a rectangular cylinder. Investigation of free rotation of elliptic cylinder across the uniform flow showed that vortex shedding causes two opposite impacts on autorotation depending on the Reynolds number, including retarded or favourable rotation[9]. Existence of premature or delayed shedding in the retarding period caused an asymmetric flow around the retreating edge, which in turn resulted in low pressure at that region and an adverse effect on the autorotation. It was also reported that a cylinder with sharper edge strengthens the attached vortex behind the retreating edge and helps autorotation.

Autorotation of multiple cylinders and their interaction in the passage of flow has also been investigated in the literature. Wang et al. [10] numerically studied the effect of spacing ratio on the dynamic behaviour and vertical structure of two tandem rotatable triangular cylinders placed in a laminar viscous flow. Three different motion states were observed by increase of the spacing ratio. When the cylinders were close, vortex shedding from the upstream cylinder was completely suppressed which resulted in low-amplitude oscillations in both cylinders. An intermediate spacing caused recovery of vortex shedding and multi-period autorotation in both cylinders. For sufficiently high amounts of spacing ratio, the interaction between two cylinders was weakened which caused more irregularity and randomness in the problem dynamics. Numerical investigation of flow field and rotational dynamics for two identical square cylinders arranged in tandem was carried out by Shao et al. [11]. Either of two cylinders was considered to be fixed or freely rotatable. The results indicated that the upstream cylinder was crucial on the system dynamics. Whether the trailing cylinder was fixed or rotating, keeping the leading cylinder in a fixed condition stabilized the flow and reduced the ratio of mean drag coefficient to the RMS of lift coefficient for both cylinders.

Regarding flow-induced rotation of wings and plates, several experimental and numerical studies have been conducted. Most of researchers have utilized a single plate or wing in their works, because of its higher rotational performance in comparison with that of triple and cruciform plates. Smith [1] experimentally examined autorotation of a flat wing and revealed that in case of too small moment of inertia, angular momentum of the wing was not sufficient to pass it through the stalled zone, and consequently the wing could not experience autorotation. It was further experimentally reported by Bakhshandeh Rostami [12] that fluttering (oscillating) motion of plates could be translated to a continuous autorotation by sufficient amount of mass moment of inertia, though a chaotic behaviour may occur during transition between pure oscillation and autorotation.

Although numerous studies have been conducted to examine autorotation of various geometries and blades across classic flow fields, there is a scarcity of studies regarding autorotation of blades within lid-driven cavity flow. Accordingly, the present study aims to investigate rotational modes and flow field in a lid-driven cavity with an elliptic blade located at its center. This study considers a high-Reynolds flow condition with higher extent of unsteadiness compared to our findings in the previous study for low-Reynolds problem [13]. The flow is simulated by immersed boundary method in which moving blade boundary conditions are imposed to the governing equations of fluid flow discretized on a regular Cartesian grid.

2. Problem statement and governing equations

This study examines a rigid elliptic blade in a lid-driven cavity flow which is only allowed to rotate freely about its centroid because of fluid-structure interaction (Figure 1). Small-to-large diameter ratio of the blade is considered to be a fixed value, $\delta/D = 0.05$, while the aspect ratio defined as D/L_0 takes four different values (0.5, 0.7, 0.8 and 0.9). The blade-fluid density ratio (ρ_s/ρ_f) is considered to be 1.1.

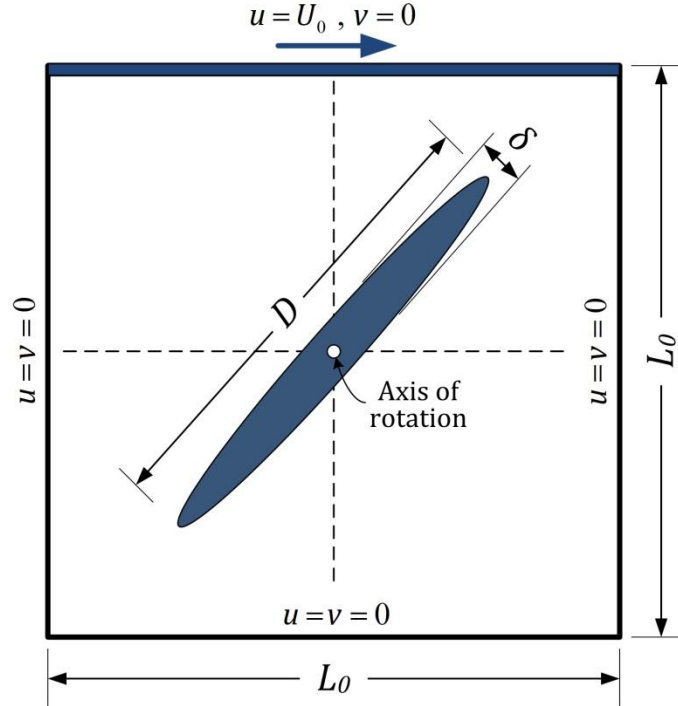


Fig. 1. Geometrical characteristics and boundary conditions [13].

Dimensionless continuity and Navier-Stokes equations for incompressible Newtonian fluid flow can be expressed as follows:

$$\nabla \cdot \mathbf{u} = 0, \quad (1)$$

$$\frac{\partial \mathbf{u}}{\partial t} + \mathbf{u} \cdot \nabla \mathbf{u} = -\nabla p + \frac{1}{Re} \nabla^2 \mathbf{u} + \mathbf{f}^*. \quad (2)$$

where \mathbf{u} and p notify normalized velocity and pressure ($\mathbf{u} = \mathbf{U}/U_0$ and $p = P/\rho U_0^2$, where \mathbf{U} , P and U_0 are velocity vector, pressure field and cavity upper wall velocity. The Reynolds number is expressed as $Re = \rho U_0 L_0 / \mu$, in which L_0 represents characteristic length. $\mathbf{x} = \mathbf{X}/L_0$ and $t = t U_0 / L_0$ indicate normalized coordinate vector and time, respectively. \mathbf{f}^* expresses an external momentum source term to impose the no-slip boundary condition in the IBM.

Structural dynamics equation for the free-to-rotate rigid blade can be expressed as follows:

$$\sum_{IB=1}^{N_b} (\mathbf{r}_{IB} \times \mathbf{f}_{IB}) = I \boldsymbol{\alpha}, \quad (3)$$

where I , $\boldsymbol{\alpha}$ and \mathbf{r}_{IB} represent blade moment of inertia, angular acceleration vector and spatial vector originated from the rotational axis and terminated at the immersed boundary point \mathbf{f}_{IB} for N_b IB points.

3. Methodology

Several revisions have been proposed for immersed boundary method to enhance its performance. The feedback forcing and direct forcing approaches are two conventional schemes in this regard. The feedback forcing can handle fluid-structure interactions in either stationary or moving boundary problems. However, it suffers considerably from numerical instabilities. In contrast, the direct forcing methodology resolves this issue by applying interpolation/distribution functions on the momentum equation [14], and it is capable in handling complicated and moving boundary problems.

The boundary effects (boundary conditions) in IBM are applied indirectly through the source terms. Two types of nodes participate in the simulation: 1) these called Lagrangian nodes nearby the solid boundary in which the source terms are calculated; 2) the grid nodes at the fluid interior region known as the Eulerian nodes. The source terms are first computed on the Lagrangian nodes and then scattered over the Eulerian nodes using a distribution function. Subsequently, the governing equations can be solved based on these employed source terms.

The current study utilizes the IBM approach employed and developed in our previous studies [13, 15-17] to simulate the fluid-structure interaction problem described in section 2. Second-order Adams-Bashforth temporal-spatial discretization of the momentum equation (Equation (2)) via the IBM leads to:

$$\mathbf{u}^{n+1} = \mathbf{u}^n + \delta t \left(\frac{3}{2} \mathbf{h}_m^n - \frac{1}{2} \mathbf{h}_m^{n-1} - \frac{3}{2} \nabla p^{n+1} + \frac{1}{2} \nabla p^n \right) + (\mathbf{f}^*)^{n+\frac{1}{2}} \delta t \quad (4)$$

where, $\mathbf{h}_m = -\mathbf{u} \cdot \nabla \mathbf{u} + \frac{1}{Re} \nabla^2 \mathbf{u}$ represents overall contribution of advection and diffusion terms. Projection of velocity field from the Eulerian nodes into the IB points and vice versa is carried out using an integration function, $I(\phi)$ and a distribution function, $D(\phi)$, respectively.

The procedure aims to compute \mathbf{f}^* based on boundary conditions and governing equations such that the boundary conditions could be applied indirectly to the Lagrangian nodes. The velocity boundary condition at the Lagrangian nodes can be obtained from the integration function, as follows:

$$\mathbf{U}_r^{n+1} = I(\mathbf{u}^{n+1}). \quad (5)$$

An intermediate velocity, \mathbf{u}^* is also defined which is useful in the numerical procedure:

$$\mathbf{u}^* = \mathbf{u}^n + \delta t \left(\frac{3}{2} \mathbf{h}_m^n - \frac{1}{2} \mathbf{h}_m^{n-1} + \frac{1}{2} \nabla p^n \right). \quad (6)$$

The velocity at IB points can be expressed based on Equations (4)-(6), as follows:

$$\mathbf{U}_r^{n+1} = I(\mathbf{u}^{n+1}) = I \left(\mathbf{u}^* - \frac{3}{2} \nabla p^{n+1} \right) + I \left(\mathbf{f}^{*n+\frac{1}{2}} \delta t \right). \quad (7)$$

Let's $\mathbf{F}_r^* = I \left(\mathbf{f}^{*n+\frac{1}{2}} \delta t \right)$, then Equation (7) is written as:

$$\mathbf{F}_r^* = \mathbf{U}_r^{n+1} - I \left(\mathbf{u}^* - \frac{3}{2} \nabla p^{n+1} \right). \quad (8)$$

Using the distribution function, the force source term can be mapped on the Eulerian nodes:

$$(\mathbf{f}^*)^{n+\frac{1}{2}} \delta t = D(\mathbf{F}_r^*) = D \left(\mathbf{U}_r^{n+1} - I \left(\mathbf{u}^* - \frac{3}{2} \nabla p^{n+1} \right) \right) \quad (9)$$

This source term can be applied to the Cartesian grid nodes in order to impose the solid boundary conditions. The

details of fluid-solid equation coupling and numerical algorithm can be found in our previous study [13].

4. Results and Discussion

In order to analyze flow field and autorotation of the blade in the lid-driven cavity, the following results are presented in the current section:

- streamlines for three selected dimensionless times, i.e. $t = 20, 80, 150$
- temporal variation of blade rotation angle in radian, i.e. $\phi - t$ plot
- temporal variation of dimensionless rotational speed of the blade, i.e. $\omega^* - t$ plot, where $\omega^* = \omega L_0 / U_0$
- temporal variation of dimensionless moment applied on the blade, i.e. $C_T - t$ plot, where $C_T = T / (\rho U_0^2 L_0^3 / 4)$

Based on the literature, cavity flow simulation has been reported to be stable and steady when Reynolds number is as large as 21,000 and computational grid is sufficiently fine [18]. In order to check if the grid is adequately fine, grid independency test is first carried out, and then near-wall y^+ is calculated when $Re = 20,000$. The results for six simulations with different grid resolutions from 101×101 to 601×601 have indicated that increase of grid resolution from 351×351 to 601×601 only causes 0.11% of deviation in the dimensionless rotational speed, which indicates numerical convergence of flow field. Additionally, y^+ is calculated based on $y^+ = u^* y / \nu$, in which u^* denotes friction velocity, obtained as $u^* = (C_f U_0^2 / 2)^{1/2}$ where skin friction coefficient C_f is estimated from Schlichting's correlation, $C_f = 2(\log_{10} Re_{L_0} - 0.65)^{-2.3}$ [19]. The largest estimate of y^+ is obtained to be 10.5 for the 101×101 grid and 1.8 for the 601×601 grid resolutions. Since y^+ is close to unity, particularly in the case of fine grids, computational grid is fine enough to capture vortical flow structures and flow unsteadiness when $Re = 20,000$.

Prior to analysis of flow field and dynamic evolution of blade, three influential vortex types in this study are classified as follows (as illustrated in Figure 2):

- Type-A vortex as a large-scale and energetic flow structure is generally available in the lid-driven cavity flow. This vortex is produced by movement of the cavity upper wall.
- Type-B vortices (also termed as side vortices) are generated due to interaction between fluid flow and the inertial blade. Such vortices are mostly observed downstream of the leeward sides of the blade.
- Type-C vortices are formed as the result of co-rotating side vortices at both sides of the blade surface. These vortices are located at the central region of the cavity. In contrast to clockwise rotational direction of type-A and type-B vortices, type-C vortex spins in the counter-clockwise direction.

By enlargement and intensification of a vortex, contribution of other vortices decreases, and the flow field is therefore characterized by the larger vortex.

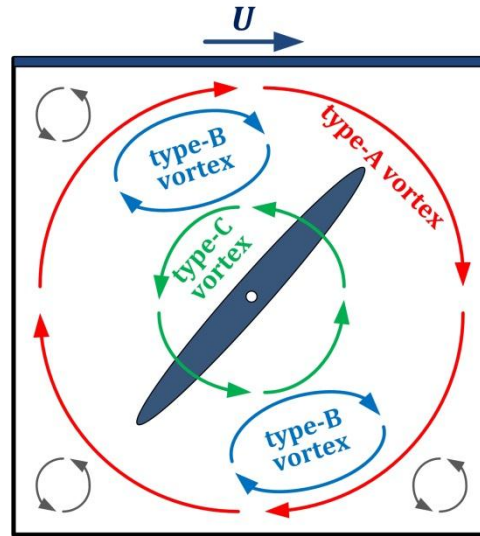


Fig. 2. General visualization of three influential vortex types of the flow field [13].

Figure 3 presents the streamlines of the cavity flow at $Re = 20000$ for four different blade lengths $D/L_0 = 0.5, 0.7, 0.8, 0.9$ at three different dimensionless times ($t = 20, 80, 150$). The $\phi - t$, $\omega^* - t$ and $C_T - t$ plots for the four mentioned blade lengths are demonstrated in Figure 4. Because of relatively high Reynolds number, flow instability increases and larger number of small-scale vortices can be observed nearby the blade and at the cavity corner zones. This can be effective on generation and evolution of the main vortices of the cavity flow and can characterize the blade dynamics.

In the initial temporal stage of the case $D/L_0 = 0.5$, the blade mainly rotates in the clockwise direction due to dominance of the type-A vortex. However, as Figures 4(b) and 4(c) show, some sharp variations can be observed in both rotational speed and blade moment when $t < 40$. Such unsteadiness can be due to inconsistency of the blade rotational speed and the fluid velocity field, and generation of some local small-scale vortices which considerably deform the type-A vortex from its ordinary topology (as can be seen in Figure 3(a) at $t = 20$). By evolution of flow structures and enhancement of their matching with the blade movement, the type-B vortices are generated nearby the blade surface (see Figure 3(b) at $t = 80$). These vortices eventually lead to generation of the counter-rotating type-C vortex at the central region of the cavity, as can be seen in Figure 3(c) at $t = 150$. Because of short length of the blade, it is effectively characterized by this central vortex. Figures 4(a) and 4(b) indicate that after the initial stage and at about $t = 50$, the blade spin direction changes and it starts to rotate in the counter-clockwise direction. By generation and intensification of the side vortices, and in particular the central type-C vortex, the rotational speed gradually increases until approaching a regular oscillating pattern with a constant mean at $t > 100$. Such regular oscillations are induced by the cyclic moment applied to the blade in the respective period, as illustrated in Figure 4(c).

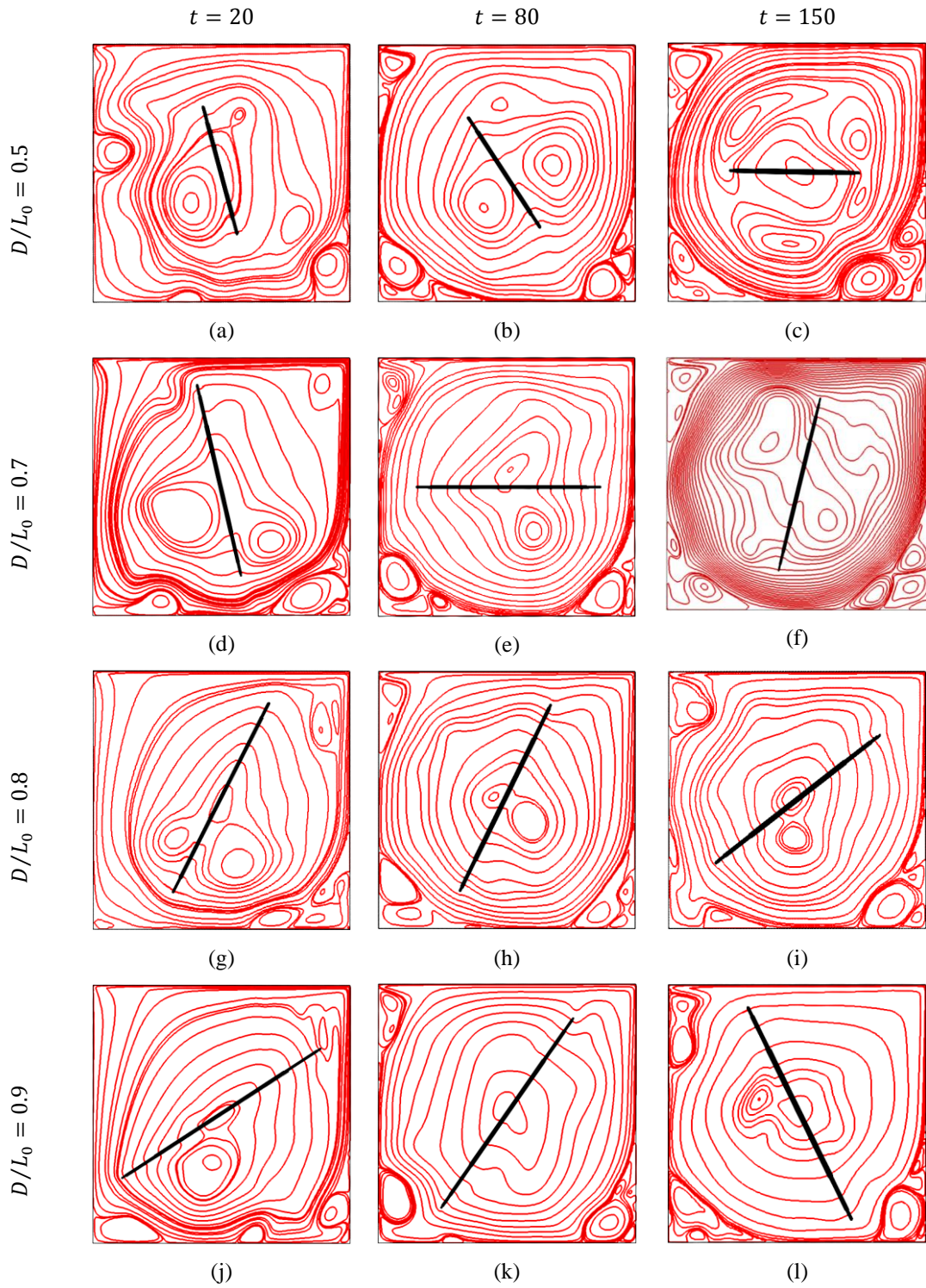


Fig. 3. Streamline patterns around the blade at $Re = 20000$ for four different blade lengths and three different dimensionless times.

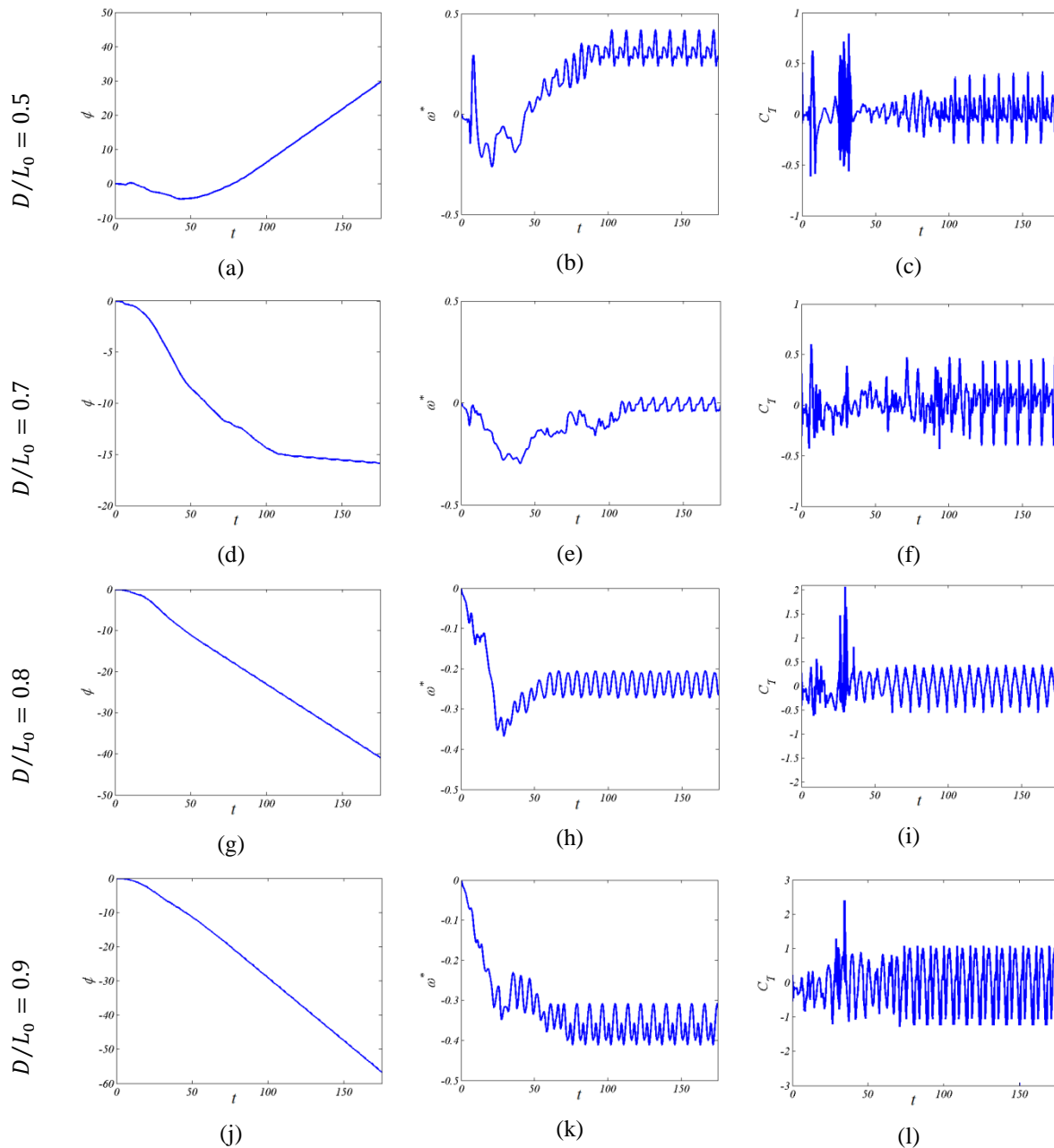


Fig. 4. Temporal variation of blade angle ϕ (the left column), rotational speed ω^* (the middle column) and blade moment C_T (the right column) with dimensionless time at $Re = 20000$, for four different blade lengths.

In the case of $D/L_0 = 0.7$, the blade is large enough to generate the type-B vortices at the initial temporal stage, as can be seen in Figure 3(d) at $t = 20$. In this stage, blade starts to rotate in the clockwise direction due to dominance of the energetic type-A vortex. By passing the time, the side vortices intensify and shift towards the blade rotational axis (as illustrated in Figures 3(e) and 3(f) for $t = 80$ and $t = 150$, respectively). Although the type-A vortex applies a favourable clockwise moment, such flow structure evolution results in an opposing moment that gradually decreases the blade rotational speed (Figures 4(d) and 4(e)). After about $t = 100$, these moments are balanced, and just cyclic variation of the blade moment around zero value can be observed from Figure 4(f). According to Figures 4(d) and 4(e), such stage corresponds to regular small-amplitude fluttering of the blade at a fixed angular orientation.

In the cases of $D/L_0 = 0.8, 0.9$, the blade is sufficiently large and it is dominantly characterized by the large-scale type-A vortex. The steady descending trend of the angle of rotation in Figures 4(g) and 4(j) reveals that clockwise autorotation is the principal dynamic mode for these two blade configurations. Figures 4(h) and 4(k) show that after some irregular variations of the blade rotational speed at the initial stage, ω^* approaches to a stable condition with regular oscillations around a constant negative (clockwise) mean value. This constant value as well as frequency and amplitude of oscillations are greater in the case of $D/L_0 = 0.9$ compared to those of the case $D/L_0 = 0.8$. This is because of higher interaction between the type-A vortex and the blade for a longer blade that enhances both of the blade moment and unsteadiness level of flow structures.

Considerable similarities can be observed between streamlines of the cases $D/L_0 = 0.8, 0.9$ at each dimensionless time (Figures 3(g) to 3(l)). It is evident that the large-scale type-A vortex is the dominant flow structure, while small-scale type-B vortices are also available in most of snapshots. Due to higher inconsistency of flow field with the blade dynamics at the initial temporal stage, the side vortices have larger scales at $t = 20$ (Figures 3(g) and 3(j)) in comparison with the later times. As time passes, the side vortices shift towards the central zone and weaken. As a result, dominance of the type-A vortex on the fluid-blade interaction enhances, and the blade rotational speed in the clockwise direction increases. In comparison with the streamlines observed for $Re = 12000$, the results for $Re = 20000$ involve higher unsteady interactions. The small-scale side vortex at the central region of Figure 3(l) (corresponding to $D/L_0 = 0.9$ at $t = 150$) is an indication of such unsteadiness. Such weak vortices were observed periodically during the blade autorotation.

Figure 5 presents the polar plots of ω^* with respect to ϕ for $Re = 20000$ and three different blade lengths, $D/L_0 = 0.5, 0.8, 0.9$. These three geometries correspond to steady autorotation modes of the blade in the counter-clockwise direction ($D/L_0 = 0.5$) or the clockwise direction ($D/L_0 = 0.8, 0.9$). In the case of $D/L_0 = 0.5$, two major peaks can be observed at $\phi = 45^\circ$ and 255° , and the curve is wavy in other circumferential positions (Figure 5(a)). This wavy characteristic is due to short length of the blade. In other words, utilization of a shorter blade decreases the impact of principal type-A vortex on the blade while it increases the effect of more unsteady vortices (such as the type-B and type-C vortices) on the blade. However, by increase of the blade length, the blade dominantly interacts with the more stable type-A vortex. As can be seen in Figure 5(b) and 5(c), in the cases $D/L_0 = 0.8$ and 0.9 , four peaks occur at about $\phi = 90^\circ, 180^\circ, 270^\circ$ and 360° which correspond to the blade orientations with the smallest distance to the cavity surface and the highest level of interaction with the type-A vortex. Some slight deviation of the peaks position with respect to the orientations $\phi = 90^\circ, 180^\circ, 270^\circ$ and 360° are due to periodic generation of small-scale vortices nearby the blade at this high-Reynolds flow condition.

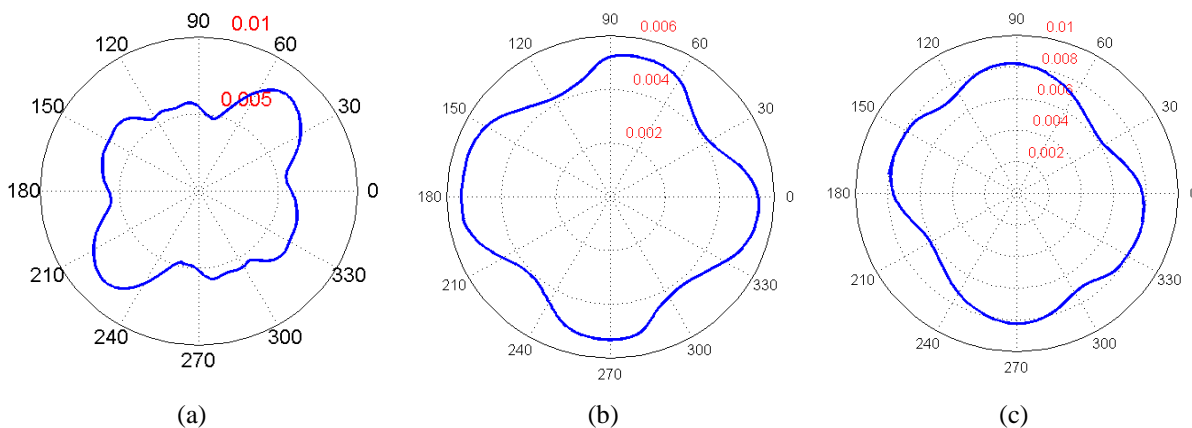


Fig. 5. Polar plots of the dimensionless rotational speed ω^* relative to the angle of rotation ϕ for $Re = 20000$ during the regular autorotation stage of three different blade lengths: (a) $D/L_0 = 0.5$; (b) $D/L_0 = 0.8$; (c) $D/L_0 = 0.9$.

5. Conclusions

In this study, vortex-induced auto-rotation of an elliptic blade due to lid-driven cavity was investigated. Iterative direct forcing immersed boundary method was employed to impose the moving blade boundary conditions to the governing equations of fluid flow on a regular Cartesian grid. The equations were discretized by the second-order Adams-Bashforth temporal-spatial scheme in order to provide the system of equations required for solving the fluid-solid interaction problem. Three types of vortices were principally effective on the blade dynamics: the large-scale type-A vortex rotating in the clockwise direction due to movement of the cavity upper wall; the co-rotating type-B side vortices generated by interaction between cavity flow and inertial blade; the central type-C vortex spinning in the counter-clockwise direction produced by the side vortices. Examination of flow and dynamic characteristics for four different blade lengths and a high-Reynolds condition ($Re = 20,000$) revealed the following concluding remarks:

- In the case of short blade ($D/L_0 = 0.5$), the blade was dominated by central type-C vortex, and consequently it exposed to counter-clockwise moment leading to steady autorotation in the same direction.
- Intensification of side vortices in the case of $D/L_0 = 0.7$ led to relatively balanced impact of clockwise and counter-clockwise moments on the blade. Accordingly, the steady dynamic mode of blade was small-amplitude fluttering at a fixed angular orientation.
- For longer blade configurations, i.e. $D/L_0 = 0.8, 0.9$, the blade was dominantly exposed to large-scale energetic type-A vortex, with a powerful clockwise moment. This caused persistent autorotation in the same direction, with regular oscillations around a constant mean value, which were induced by flow unsteadiness due to fairly large value of Reynolds number.

References

- [1] E. Smith, Autorotating wings: an experimental investigation, *Journal of Fluid Mechanics*, 50(3) (1971) 513-534.
- [2] H. Juarez, R. Scott, R. Metcalfe, B. Bagheri, Direct simulation of freely rotating cylinders in viscous flows by high-order finite element methods, *Computers & Fluids*, 29(5) (2000) 547-582.
- [3] Y. Xia, J. Lin, X. Ku, T. Chan, Shear-induced autorotation of freely rotatable cylinder in a channel flow at moderate Reynolds number, *Physics of Fluids*, 30(4) (2018) 043303.
- [4] Y. Xia, J. Lin, X. Ku, Flow-induced rotation of circular cylinder in Poiseuille flow of power-law fluids, *Journal of Non-Newtonian Fluid Mechanics*, 260 (2018) 120-132.
- [5] B. Skews, Autorotation of many-sided bodies in an airstream, *Nature*, 352(6335) (1991) 512-513.
- [6] T. Zaki, M. Sen, M. Gad-el-Hak, Numerical and experimental investigation of flow past a freely rotatable square cylinder, *Journal of Fluids and structures*, 8(6) (1994) 555-582.
- [7] S. Ryu, Quadrant analysis on vortex-induced autorotation of a rigid square cylinder, *Journal of Mechanical Science and Technology*, 32(6) (2018) 2629-2635.
- [8] Y.G. Park, G. Min, M.Y. Ha, H.S. Yoon, Response characteristics of vortex around the fixed and freely rotating rectangular cylinder with different width to height ratios, *Progress in Computational Fluid Dynamics, an International Journal*, 15(1) (2015) 1-9.

- [9] H.J. Lugt, Autorotation of an elliptic cylinder about an axis perpendicular to the flow, *Journal of Fluid Mechanics*, 99(4) (1980) 817-840.
- [10] S. Wang, L. Zhu, X. Zhang, G. He, Flow past two freely rotatable triangular cylinders in tandem arrangement, *Journal of fluids engineering*, 133(8) (2011).
- [11] J. Shao, C. Shu, N. Liu, X. Zhao, Numerical investigation of vortex induced rotation of two square cylinders in tandem arrangement, *Ocean Engineering*, 171 (2019) 485-495.
- [12] A. Bakhshandeh Rostami, Hydrokinetic energy harvesting by autorotation of a plate with hinged axis, PhD Thesis, Federal University of Rio de Janeiro, Brazil, 2015.
- [13] A.A. Hosseinjani, G. Akbari, Numerical study of vortex-induced autorotation of an elliptic blade in lid-driven cavity flow, *Fluid Dynamics Research*, 54(6) (2022).
- [14] C. Ji, A. Munjiza, J. Williams, A novel iterative direct-forcing immersed boundary method and its finite volume applications, *Journal of Computational Physics*, 231(4) (2012) 1797-1821.
- [15] A.A. Hosseinjani, A. Ashrafizadeh, An extended iterative direct-forcing immersed boundary method in thermo-fluid problems with Dirichlet or Neumann boundary conditions, *Journal of Central South University*, 24(1) (2017) 137-154.
- [16] A.A. Hosseinjani, A. Ashrafizadeh, Flow confinement effects on the wake structure behind a pitching airfoil: a numerical study using an immersed boundary method, *Journal of Bionic Engineering*, 14(1) (2017) 88-98.
- [17] A.A. Hosseinjani, M. Nikfar, Numerical analysis of unsteady natural convection from two heated cylinders inside a rhombus enclosure filled with Cu-water nanofluid, *International Communications in Heat and Mass Transfer*, 113 (2020) 104510.
- [18] E. Erturk, T.C. Corke, C. Gökçöl, Numerical solutions of 2- D steady incompressible driven cavity flow at high Reynolds numbers, *International journal for Numerical Methods in fluids*, 48(7) (2005) 747-774.
- [19] H. Schlichting, *Boundary layer theory*, McGraw-Hill, New York, 1979.